Superconductor-insulator transition driven by pressure-tuned intergrain coupling in nanodiamond films

Gufei Zhang,[1,*,†] Yonghui Zhou,[2,*] Svetlana Korneychuk,[3,*] Tomas Samuely,[4] Liwang Liu,[5] Paul W. May,[6] Zheng Xu,[7] Oleksandr Onufriienko,[4] Xuefeng Zhang,[8] Johan Verbeeck,[3] Peter Samuely,[4] Victor V. Moshchalkov,[9] Zhaorong Yang,[2,10,11,‡] and Horst-Günter Rubahn[1]

[1]*NanoSYD, Mads Clausen Institute and DIAS Danish Institute for Advanced Study, University of Southern Denmark, Alsion 2, DK-6400 Sonderborg, Denmark*

[2]*Anhui Province Key Laboratory of Condensed Matter Physics at Extreme Conditions, High Magnetic Field Laboratory, Chinese Academy of Sciences, Hefei 230031, China*

[3]*EMAT, University of Antwerp, Groenenborgerlaan 171, B-2020 Antwerp, Belgium*

[4]*Centre of Low Temperature Physics, Institute of Experimental Physics, Slovak Academy of Sciences & Faculty of Science, P. J. Safarik University, Kosice, Slovakia*

[5]*Laboratory for Soft Matter and Biophysics, Department of Physics and Astronomy, KU Leuven, B-3001 Heverlee, Belgium*

[6]*School of Chemistry, University of Bristol, Bristol BS8 1TS, United Kingdom*

[7]*School of Electrical and Computer Engineering, University of California, Davis, California 95616, USA*

[8]*Innovative Center for Advanced Materials, Hangzhou Dianzi University, 310012 Hangzhou, China*

[9]*Institute for Nanoscale Physics and Chemistry, KU Leuven, B-3001 Heverlee, Belgium*

[10]*Collaborative Innovation Center of Advanced Microstructures, Nanjing University, Nanjing 210093, China*

[11]*Institute of Physical Science and Information Technology, Anhui University, Hefei 230601, China*

(Received 3 December 2018; revised manuscript received 30 January 2019; published 5 March 2019)

We report on the pressure-driven superconductor-insulator transition in heavily boron-doped nanodiamond films. By systematically increasing the pressure, we suppress the Josephson coupling between the superconducting nanodiamond grains. The diminished intergrain coupling gives rise to an overall insulating state in the films, which is interpreted in the framework of a parallel-series circuit model to be the result of bosonic insulators with preserved localized intragrain superconducting order parameters. Our investigation opens up perspectives for the application of high pressure in research on quantum confinement and coherence. Our data unveil the percolative nature of the electrical transport in nanodiamond films, and highlight the essential role of grain boundaries in determining the electronic properties of this material.

DOI: 10.1103/PhysRevMaterials.3.034801

I. INTRODUCTION

The wide-ranging electronic properties of lab-grown diamond coupled with its high thermal conductivity make it a superior material for a potentially disruptive technology for the post-silicon era. The industrial interest for diamond stems from not only its unique intrinsic properties such as its extraordinarily high stiffness and thermal conductivity but also its wide-ranging electronic properties [1,2]. With recent advances in diamond growth technology and the benefits of industrial scale up, lab-grown diamond is nowadays a low-cost material and the basis for a multimillion-dollar industry providing drill bits for machinery and mining. Owing to the development of chemical vapor deposition (CVD) processes for the growth of diamond thin films, the range of applications for diamond has increased hugely. This is of special importance for the electronics industry where diamond layers with vastly different electronic properties (highly insulating when undoped, semiconducting when lightly boron-doped, and metallic when heavily boron-doped) can be deposited and etched into miniaturized high-technology components [3,4].

The discovery of superconductivity in heavily boron-doped diamond in 2004 not only opened additional perspectives for the applications of this material [5,6], e.g., diamond-based superconducting quantum interference devices [7], but also stimulated fundamental research on superconductivity in doped insulators [8]. The emergence of superconductivity in boron-doped diamond itself is an intriguing phenomenon, and the origin of the superconductivity still remains an open question. Scanning tunneling microscopy (STM) data suggest that diamond is a Bardeen-Cooper-Schrieffer (BCS) superconductor due to the match between the experimental values and the theoretical prediction of the BCS ratio $2\Delta_0 k_B T_c = 3.52$, where $2\Delta_0$ is the zero-temperature superconducting gap size, k_B is the Boltzmann constant, and T_c is the superconducting transition temperature. In contradiction, the fact that the emergence of superconductivity is accompanied by the doping-driven insulator-metal transition in this material points to the relevance of the resonant valence band theory, where singlet coupling between the spins of neighboring boron acceptors gives rise to the Cooper pairing [9,10].

Much effort has been devoted to studying the electronic correlations in lab-grown diamond as a function of different

*These authors contributed equally to this work.
†gufei@mci.sdu.dk
‡zryang@issp.ac.cn

parameters. For instance, detailed surveys have been devoted to the dependence of the insulator-metal transition and the superconducting transition temperature on the boron doping level. When increasing the boron concentration, an increase and a decrease in T_c have been reported for underdoped and overdoped diamond films, respectively [11,12]. The influence of film thickness on the electronic properties has been monitored from the micrometer down to the nanometer length scales, where no reduction of T_c was found despite the reduced dimensionality [13]. Recently, pressure-induced suppression of T_c and structural transformation of the grain boundaries have been reported for a freestanding 60 μm-thick diamond film [14]. Apart from these studies focused on the boron-doped diamond material itself, a series of investigations carried out with an emphasis on the role of granular morphology in the confinement and coherence of the superconducting order parameter in lab-grown diamond has unveiled various anomalous quantum phenomena such as the bosonic insulating state [15–17]. Due to the seeding procedure used for CVD diamond growth onto nondiamond substrates, lab-grown diamond is generally granularly disordered, where relatively pure diamond crystallites are self-assembled and joined together by grain boundaries composed of a mixture of sp^2, sp^3, and amorphous carbon. Thus, CVD diamond can be considered to be a disordered network of quantum wells [18]. Being able to tune the granular disorder will, therefore, be a powerful platform for research on quantum confinement and coherence effects. Nevertheless, the measures for adjusting the intergrain coupling and thus tuning the quantum confinement and coherence have so far been limited to modifying the mean intergrain distance by using colloidal suspensions of diamond nanoparticles with different degrees of dilution for seeding [17].

Here, we report on our observations of the pressure-driven superconductor-insulator transition in heavily boron-doped nanodiamond thin films. In contrast to the conventional applications of high-pressure techniques in studies of the electronic structures of condensed matter, we use the technique as an efficient tool to tune the intergrain coupling in 600-nm-thick freestanding nanodiamond thin films, and investigate their low-temperature phase transition and high-temperature electrical transport properties as a function of pressure in the range of 0–19.2 GPa. Since diamond withstands crushing pressures in excess of 600 GPa [19], the nanodiamond grains can persist through the pressure enhancement despite the destruction of the grain-boundary-grain Josephson junctions, making the nanodiamond film a bosonic insulator with localized intragrain Cooper pairs under high pressures. The nanodiamond films are theoretically modeled with a parallel-series combination circuit that well characterizes all the transport data across the superconductor-insulator transition. We note that our resulting picture and the theoretical model, established for nanodiamond thin films, can also be applied to general granular disordered superconductors.

II. EXPERIMENT

A. Preparation of freestanding boron-doped nanodiamond films

The heavily boron-doped nanodiamond films were grown using hot filament CVD [1]. The substrates were undoped Si (100) wafers with a 2-nm-thick native oxide layer on the surface. To generate nucleation sites for diamond growth, these substrates were seeded with colloidal suspensions of diamond nanoparticles (diameter ~20 nm) using an electrospray process [20] (seeding density $\sim 3 \times 10^{10}$ cm^{-2} as estimated by scanning electron microscopy). The seeded substrate was then placed 3 mm below a 2200 °C tantalum filament in the CVD reactor. A gas mixture of 0.6% CH_4 in H (total flow 200 sccm) was thermally dissociated using the hot filament for diamond growth onto the substrate, which was maintained at 800 °C. Boron doping was realized by adding diborane (B_2H_6) to the gas mixture with a B_2H_6/CH_4 ratio of 5%, which previous experiments have shown to result in heavily boron-doped diamond with metallic conductivity. During the growth process, the isolated diamond seeds enlarge, and after about 15 min they coalesce into a continuous polycrystalline diamond thin film that continues to increase in thickness with time. Growth was stopped after 40 min resulting in a 600-nm-thick continuous thin film [17]. For the electrical transport measurements under high pressure, these samples were submerged in a HF bath for 24 h to etch the SiO_2 layer, allowing the freestanding nanodiamond thin films to chemically peel off the substrate.

B. Structural analysis using transmission electron microscopy

A structural analysis of the nanodiamond films was carried out using annular dark-field scanning transmission electron microscopy (ADF-STEM) and spatially resolved electron energy-loss spectroscopy (STEM-EELS). Samples that were thin enough for TEM were prepared by milling the nanodiamond films with a focused ion beam. To protect the nanodiamond surface from ion beam damage, a layer of Pt was deposited prior to the ion milling. STEM was performed on a FEI cubed Titan instrument equipped with a probe corrector using an acceleration voltage of 300 kV. EELS was performed at 300 kV making use of a Gatan Enfinium electron spectrometer. ADF imaging was carried out with a convergence semiangle $\alpha \sim 21$ mrad. STEM-EELS maps were obtained with the same convergence angle and with collection angle 100 mrad. Quantitative estimation of the boron concentration was made using the EELSMODEL software with parameters of convergence angle 20 mrad, collection angle 80 mrad, and spectral energy resolution 1 eV.

C. Electrical transport measurements under different pressures

The nanodiamond films were first measured using a Physical Property Measurement System (Quantum Design) with the sample chamber pumped down to high vacuum. High-pressure electrical transport measurements were conducted in a screw-pressure-type diamond anvil cell made of BeCu alloy. A pair of anvil culets with a diameter of 500 μm were used to generate high pressure. A T301 stainless-steel gasket was preindented from a thickness of 200–50 μm, in which a 500-μm-wide hole was drilled in the center. A mixture of epoxy and fine cubic boron nitride (c-BN) powders was compressed firmly to insulate the electrodes from the stainless-steel gasket. Another hole of 180 μm in diameter was then drilled in the center of the pit, which was further

filled with soft NaCl fine powders as the pressure-transmitting medium to maintain a quasihydrostatic pressure environment. The freestanding nanodiamond film was loaded into the chamber together with some ruby powder for pressure calibration. The electrical transport properties of the film were measured with the four-probe method using Pt foil as the electrodes. Pressure was calibrated using the ruby fluorescence shift at room temperature [21].

D. Direct local measurements of the density of states

In contrast to superconductors situated in the clean limit, disordered superconductors, no matter whether they are uniformly disordered on the length scale close to atomic size or granular disordered on the grain-size scale, generally demonstrate a local superconducting transition temperature higher than the bulk value as determined by electrical transport measurements. The local superconducting transition temperature characterizes the onset of the formation of Cooper pairs in the system, while the bulk value characterizes the resistive superconducting transition.

Direct local measurements of the density of states (DOS) were performed using scanning tunneling spectroscopy to determine the local superconducting transition temperature of our nanodiamond films. The bias voltage was applied to the tip, while the sample was connected to the ground. Prior to the actual experiment, a clean Au surface was pierced with the Au tip of the STM and retracted slowly *in situ* at cryogenic temperatures. Simultaneously, the current was recorded as a function of the tip z coordinate at a constant bias voltage. This procedure was repeated until reproducible spectral features were obtained indicating typical steps corresponding to the conductance quantization and single-atom contact phenomena [22]. In this manner an atomically sharp tip was obtained, which was then positioned over the sample. The initial tunneling resistance was set to 1 MΩ.

To obtain the local differential conductance, the locally measured tunneling current *versus* bias voltage curves were numerically differentiated. Because the metallic Au tip features a constant DOS at the measured bias energies, each of the differential conductance *versus* voltage spectra reflects the local superconducting density of states (SDOS) of the sample, smeared by $\sim \pm 2k_{\mathrm{B}}T$ in energy at the respective temperature. Consequently, in the low-temperature limit, the differential conductance directly measures the SDOS of the sample. In order to extract the half-width of the superconducting energy gap Δ, the BCS model of the SDOS smeared by the temperature-dependent Fermi-Dirac function was fitted to the experimental spectra [23].

III. RESULTS

Figure 1(a) shows a scanning electron microscope (SEM) image of the upper surface of the diamond thin film made up of connected nanodiamond crystallites. The inverted pyramid-like growth mode of the nanodiamond crystallites can be seen in the ADF-STEM image of the characteristic cross section of the film [Fig. 1(b)]. To map the spatial distribution of the boron dopants and determine the boron concentration, spatially resolved STEM-EELS measurements on the cross

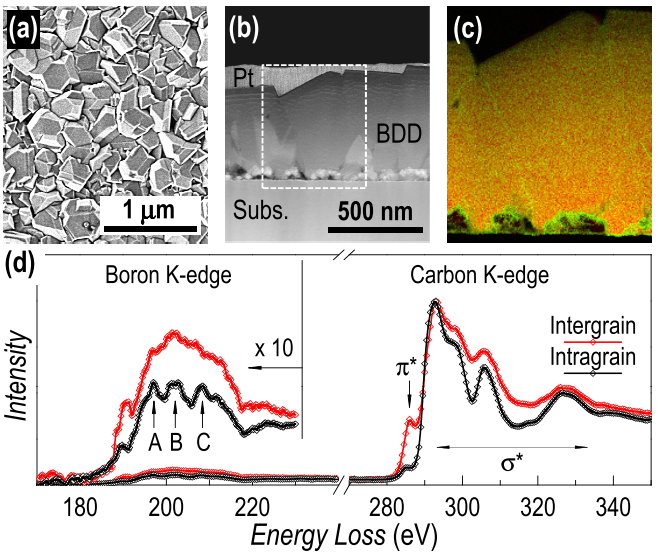

FIG. 1. Structural analysis of the heavily boron-doped nanodiamond films. (a) SEM image of the upper surface of the nanodiamond film, and (b) ADF-STEM image of its cross section. To protect the nanodiamond surface from ion milling damage during TEM sample preparation, a thin layer of Pt was deposited onto the boron-doped nanodiamond (BDD) surface. The substrate (Subs) is still present in these samples for ease of handling. (c) STEM-EELS imaging of boron (in green) and carbon (in red) distributions in the white dashed window in (b). The superposition of green and red pixels results in the yellow/orange color of the film. (d) Characteristic EELS spectra recorded from the intragrain and intergrain regions. The boron K-edge fine structures (subpeaks of A, B, and C) indicate the tetrahedral coordination of boron in nanodiamond, while the features of the boron K edge and carbon K edge are indicative of an amorphous boron/carbon mixture in the intergrain regions.

section were performed, which indicate a rather homogeneous distribution of the boron dopants in different grains and along the growth direction of the nanodiamond crystallites [Fig. 1(c)]. Analysis of the STEM-EELS data yields a boron concentration of $\sim 2 \times 10^{21}\,\mathrm{cm}^{-3}$, which is one order of magnitude higher than the critical doping level for the insulator-metal transition in boron-doped diamond [24], confirming that our nanodiamond films are heavily boron doped. As shown by the fine structures of the characteristic EELS spectra in Fig. 1(d), the nanodiamond grains are dominated by tetrahedrally coordinated boron dopants, while the grain boundaries are filled with an amorphous mixture of sp^2/sp^3 carbon and boron atoms [25].

Figure 2(a) illustrates the characteristic thermoresistivity of the nanodiamond films measured at zero applied pressure and magnetic field. Despite the heavy boron doping, the nanodiamond films exhibit a dirty metallic (or weakly insulating) normal state at high temperatures, as evidenced by the negative temperature coefficient of $\rho(T)$. The negative temperature coefficient results from the delocalization of intragrain charge carriers by thermal activation [18,26–28]. At low temperatures, a rather broad resistive superconducting transition is observed in the nanodiamond thin films with the offset critical temperature $T_{\mathrm{c}}^{\mathrm{offset}} \sim 2.3$ K [see inset in Fig. 2(a). Along with the change of the temperature coefficient of resistivity from

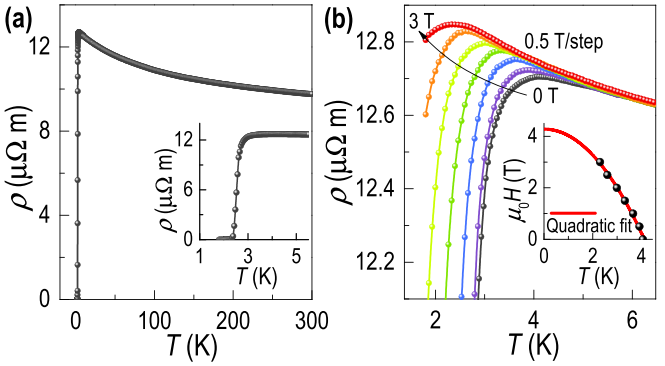

FIG. 2. Thermoresistivity of the heavily boron-doped nanodiamond films. (a) The dirty metallic (or weakly insulating) normal state and the superconducting transition of the nanodiamond film at zero magnetic field. Inset: magnification of the resistive superconducting transition. (b) Magnetic field dependence of the resistive superconducting transition. When increasing the applied magnetic field, the superconductivity is suppressed, and the $\rho(T)$ maximum is shifted towards zero temperature. Inset: quadratic fit to the $\mu_0 H$-T phase boundary for the determination of the Ginzburg-Landau coherence length.

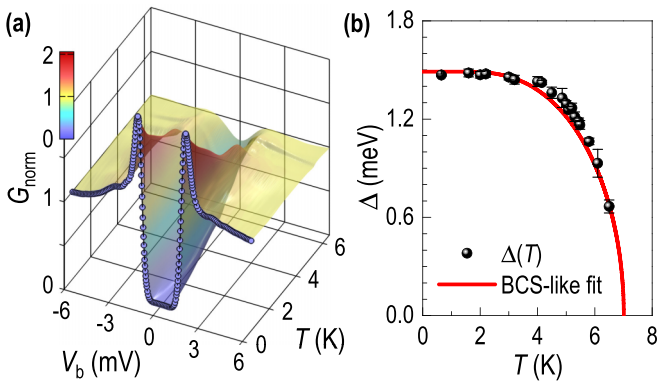

FIG. 3. Characteristic differential conductance spectra demonstrating the local density of states of the nanodiamond films. (a) Normalized tunneling conductance $G_{\rm norm}$ as a function of bias voltage $V_{\rm b}$ at different temperatures. The temperature-induced evolution of the $G_{\rm norm}(V_{\rm b})$ spectra shows the emergence of in-gap states, the decrease of the gap size, the U-V transformation of the superconducting gap, and the decline of the coherence peaks. The last two phenomena suggest the localization of remaining Cooper pairs. (b) Temperature-induced evolution of the half-width of the superconducting gap. The BCS-like fit to $\Delta(T)$ indicates the local onset critical temperature $T_{\rm c}^{\rm onset}({\rm local}) = 7\,{\rm K}$ and the zero-temperature superconducting gap $2\Delta_0 = 2.96\,{\rm meV}$.

negative to positive, $\rho(T)$ demonstrates a maximum prior to the superconducting state ($\rho = 0$) [29]. Such a $\rho(T)$ maximum has been generally observed in granular disordered superconductors. In boron-doped polycrystalline diamond films, various $\rho(T)$ maxima have been reported, e.g., a giant $\rho(T)$ peak prior to the resistive superconducting transition [15], a $\rho(T)$ bump prior to or superimposed at the transition [16,30], or in most cases a $\rho(T)$ maximum as shown in Fig. 2 [18,29]. The emergence of these $\rho(T)$ maxima can be due to the common mechanism in different systems, i.e., granular disorder-correlated localization of isolated preformed Cooper pairs [15].

To gain insight into the resistive superconducting transition, magnetic fields were applied perpendicularly to the film to suppress the superconductivity. As shown in Fig. 2(b), when increasing the applied magnetic field $\mu_0 H$, the maximum in $\rho(T)$ shifted towards zero temperature, together with the resistive superconducting transition. The crossover between the negative and positive temperature coefficients of $\rho(T)$, i.e., the maximum of $\rho(T)$, is taken as the criterion for the determination of the onset critical temperature $T_{\rm c}^{\rm onset}$ of the superconducting transition [29]. Note that this criterion provides an underestimate of $T_{\rm c}^{\rm onset}$, because in disordered systems, such as our heavily boron-doped nanodiamond thin films, Cooper pairing sets in prior to the decrease in resistivity [17]. Plotting $T_{\rm c}^{\rm onset}$ as a function of the applied magnetic field enables the $\mu_0 H$-T phase diagram to be constructed [see inset in Fig. 2(b)] Extrapolation of the quadratic fit of the $\mu_0 H$-T phase boundary yields a zero-temperature upper critical field of $\mu_0 H_{\rm c2}(0\,{\rm K}) = 4.3\,{\rm T}$ and thus the Ginzburg-Landau coherence length $\xi_{\rm GL} = [\Phi_0/2\pi H_{\rm c2}(0\,{\rm K})]^{0.5} = 8.7\,{\rm nm}$ with $\Phi_0 = h/2e$ being the flux quantum.

In contrast to the underestimate of $T_{\rm c}^{\rm onset}$ by electrical transport data, our direct local measurements of the DOS using STM/S provide a precise determination of the onset temperature of local Cooper pairing. Figure 3(a) presents the characteristic normalized differential conductance spectra, $G_{\rm norm}$, recorded from the nanodiamond films. When increasing the temperature, the U-shaped tunneling conductance, $G_{\rm norm}$, as a function of bias voltage, $V_{\rm b}$, evolves into V-shaped $G_{\rm norm}(V_{\rm b})$. The temperature-induced evolution brings about not only in-gap states, as indicated by the gradual increase of the zero-bias conductance, but also the suppression of the coherence peaks. The destruction of Cooper pairs is responsible for the emergence of the in-gap states, while the localization of remaining Cooper pairs results in the decline of the coherence peaks [17]. The half-width of the superconducting gap 2Δ is plotted *versus* temperature and fitted by the BCS-like $\Delta(T)$ dependence in Fig. 3(b). The BCS-like fit yields a local onset critical temperature $T_{\rm c}^{\rm onset}({\rm local}) = 7\,{\rm K}$ and a zero-temperature superconducting gap $2\Delta_0 = 2.96\,{\rm meV}$, which gives rise to the ratio $2\Delta_0/k_{\rm B}T_{\rm c}^{\rm onset}({\rm local}) = 4.9$. This ratio exceeds the conventional BCS theory value by 39%, indicating that our nanodiamond films are situated in the strong coupling regime.

The nanodiamond films were then placed under high pressures to investigate their electrical transport as a function of pressure in the range of 0–19.2 GPa. As shown in Fig. 4(a), when increasing the applied pressure, the normal state at high temperatures shows an enhanced resistivity and a systematic increase in the absolute value of the negative temperature coefficient of $\rho(T)$. Along with the suppressed superconducting state at low temperatures, the pronounced $\rho(T)$ enhancement extends towards zero temperature. In contrast to the 60-μm-thick diamond film studied in Ref. [14], our 600-nm-thick nanodiamond films did not exhibit pressure-induced suppression of the normal-state resistivity. The difference could be caused by the difference in film thicknesses. Note that due to the inverted pyramid-like growth mode of diamond grains [see

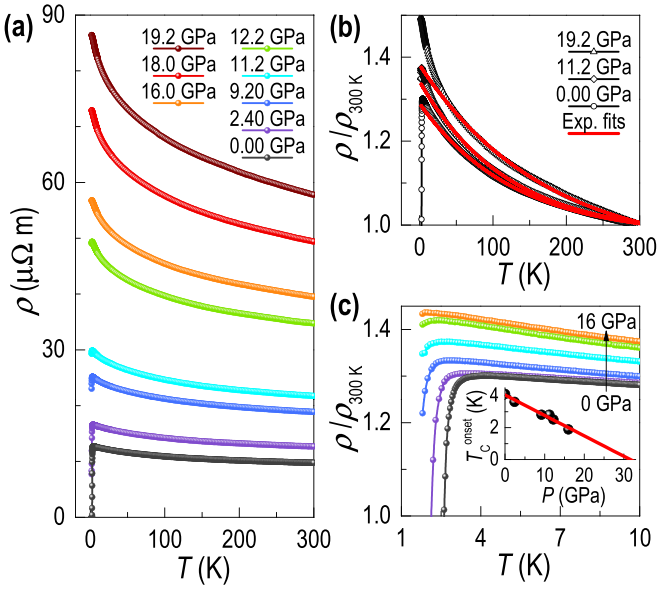

FIG. 4. Pressure-driven superconductor-insulator transition in the nanodiamond films. (a) Thermoresistivity under different pressures. The enhancement of the applied pressure results in an increase of the normal-state resistivity and a suppression of the superconducting state (curves from up to bottom: 19.2, 18.0, 16.0, 12.2, 11.2, 9.2, 2.4, and 0 GPa). (b) Exponential fits (red curves) to the thermoresistivity at high temperatures. The deviations of $\rho(T)$ from the exponential fits are indicative of the emergence of insulating states at low temperatures. (c) The influence of the applied pressure on the resistive superconducting transition. Inset: linear fit to the pressure P dependence of T_c^{onset} suggests the complete suppression of the bulk superconductivity at about 32 GPa.

Fig. 1(b)], the thicker the diamond film, the better the grains coalesce with each other, and the stiffer the film becomes. The influence of the applied pressure on the electrical transport is two-sided. On one side, the applied pressure can result in structural transformation of the grain boundaries, which lowers the resistivity [14]. On the other hand, the applied pressure can give rise to deformations/cracks at the grain boundaries, which increase the resistivity. The former apparently dominates over the latter in a thick diamond film such as the 60-μm-thick diamond film, while the latter becomes more significant in much thinner films such as our samples.

The representative $\rho(T)$ curves are normalized to their resistivity at 300 K, respectively, for comparisons [see Fig. 4(b)]. At high temperatures, $\rho(T)$ curves measured under different pressures all follow an exponential decay [18]. This exponential decay, however, does not hold at low temperatures, as indicated by the deviations of the experimental data from the exponential fits. The higher the applied pressure, the more the $\rho(T)$ overshoots the exponential law, revealing the emergence of insulating states at low temperatures under high pressures [18]. Figure 4(c) shows the influence of the applied pressure on the resistive superconducting transition. Similar to the $\rho(T)$ behavior in magnetic fields [see Fig. 2(b)] the increased pressure also shifts both the resistive superconducting transition and the $\rho(T)$ maximum towards zero temperature. As a fingerprint of the resistive superconducting transition in the presence of granular disorder, the $\rho(T)$ maxima are set as the criterion for the determination of T_c^{onset}, which is plotted as a function of the applied pressure P in the inset in Fig. 4(c). A linear fit to the T_c^{onset}-P plot yields a slope of -0.13 K/GPa and suggests the annihilation of the bulk superconductivity at about 32 GPa.

IV. DISCUSSION

Comprehension of the electrical transport properties becomes straightforward when taking into account the granular structure of the nanodiamond thin films. Due to the high concentration of tetrahedrally coordinated boron dopants, the nanodiamond grains are situated deep in the metallic regime. The metallic grains are separated by highly resistive grain boundaries rich in impurity boron atoms and a mixture of sp^2/sp^3 carbon, making the system a resistor network at high temperatures and a Josephson junction network below the superconducting transition temperature. When the grain size is of the same order of magnitude as the film thickness, the network can be treated as a two-dimensional system [30].

When applying pressure to the system, due to the extraordinarily high stiffness, the nanodiamond grains can withstand relatively high pressure and act as preservers of free charge carriers and Cooper pairs, while the amorphous grain boundaries can more easily deform or even crack under high pressures. Accordingly, the applied pressure serves as a powerful tool for tuning the intergrain coupling and thus the intragrain confinement of charge carriers and Cooper pairs [see Fig. 5(a)]. At high temperatures, the deformed/cracked grain boundaries set up energy barriers suppressing/prohibiting the tunneling of free charge carriers across the grain boundary, which gives rise to the increase in the normal-state resistivity and the absolute value of the negative temperature coefficient of resistivity.

Below T_c^{onset}(local), the deformations and cracks at the grain boundaries weaken or even destroy the Josephson junctions (weak links). As a result, it becomes more difficult to establish a percolative path for the Cooper pairs, making the condensation and thus the dissipationless flow of Cooper pairs impossible. In this case, a quasi-zero-dimensional state of Cooper pairs, which has been revealed for granular superconducting diamond films by so-called fluctuation spectroscopy [31], can set in and lead to the appearance of an overall insulating phase with localized Cooper pairs. Note that our picture, as illustrated in Fig. 5(a), is still valid in the case that the heavily boron-doped nanodiamond grains cannot withstand the applied high pressures and crack under 0–19.2 GPa. This is highly unlikely, but even so, Cooper pairs can still persist through the pressure enhancement due to the minute value of $\xi_{GL} = 8.7$ nm. In this case, the circular dots in Fig. 5(a) will stand for the cracked pieces rather than the as-grown nanodiamonds themselves.

Our picture, based on pressure-enhanced granular disorder, does not consider the existence of an intermediate metallic but normal phase, although such a phase has been reported for a set of diamond films with different boron concentrations and a superconducting diamond film irradiated at different fluences [13,32]. In contrast to our methodology, the techniques used in these two studies exert a direct and vital influence on the process of Cooper pairing itself. In the case of Ref. [13],

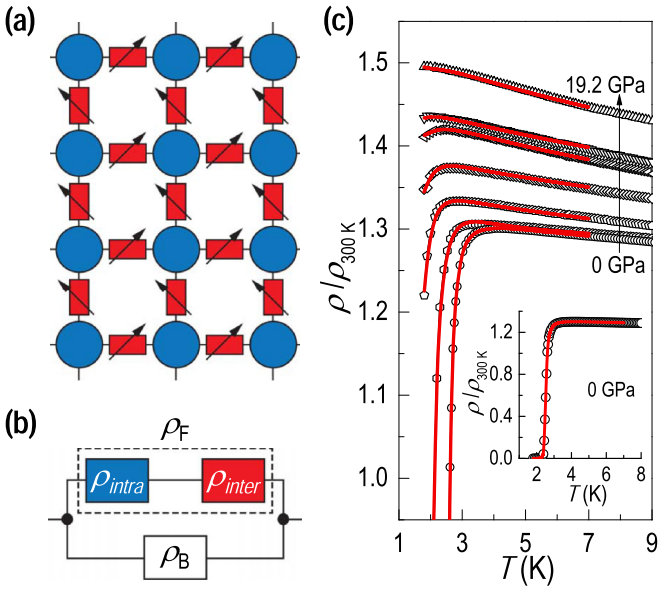

FIG. 5. Modeling of the pressure-driven superconductor-insulator transition with a series-parallel circuit. (a) Representation of the nanodiamond thin films as a resistor network. Under pressure, the nanodiamond grains (blue) are interconnected by tunable resistors (red). (b) The two-channel model, i.e., a fermionic channel (ρ_F) connected in parallel with a bosonic channel (ρ_B). The intragrain resistivity (ρ_{intra}) and the intergrain resistivity (ρ_{inter}) are connected in series to describe the fermionic channel. Accordingly, the resistor network is simplified into a parallel-series circuit. (c) Magnification of the resistive superconducting transition and the insulating state fitted by the parallel-series circuit model (red curves) (curves from top to bottom: 19.2, 16.0, 12.2, 11.2, 9.2, 2.4, and 0 GPa). Inset: the fitting covers the entire temperature range of the superconducting transition.

the intermediate metallic but normal state emerged at boron concentrations below the critical level for Cooper pairing. In the case of Ref. [32], the irradiation destroyed the Cooper pairs by generating disorder centers on atomic scale.

For the theoretical modeling of our experimental data, the resistor network is simplified into a two-channel model, i.e., a fermionic channel ρ_F connected in parallel with a bosnonic channel ρ_B [see Fig. 5(b)]. The switch-like function of this parallel circuit corresponds with the fact that Cooper pairs gradually take over the control of electrical conductivity from fermions upon the superconducting transition [16]. As shown in Fig. 5(b), we use two resistors connected in series to describe the fermionic channel, where the two resistors ρ_{intra} and ρ_{inter} represent the intragrain and intergrain resistivities, respectively. When lowering the temperature down to T_c^{onset}(local), the superconducting gap opens locally in the nanodiamond grains. In the presence of granular disorder, isolated localized Cooper pairs are formed by removing single quasiparticles around the Fermi energy from the fermionic channel. The extinction of single quasiparticles around the Fermi energy contributes to the $\rho(T)$ increase prior to the resistive superconducting transition [15,16]. At even lower temperatures, the intergrain phase coherence gives rise to the resistive superconducting transition. The $\rho(T)$ maximum appears as a crossover between the $\rho(T)$ increase and the resistive superconducting transition. When increasing the applied pressure, the contribution from the intergrain resistivity to the $\rho(T)$ increase becomes more and more important, due to the formation of deformations/cracks at the grain boundaries.

Accordingly, the fermionic channel ρ_F is written as

$$\rho_F = \rho_{intra} + \rho_{inter}. \tag{1}$$

Below T_c^{onset}(local), ρ_{intra} can be semiempirically modeled as

$$\rho_{intra} = \rho_n\left[-2\int_{\Delta(T)}^{\infty} g(E)f'(E)dE\right]^{-1}, \tag{2}$$

where $\Delta(T) = \Delta_0[1\text{-}T/T_c^{onset}(\text{local})]^{\omega}$ describes the opening of the superconducting gap (in the BCS theory, $\omega = 0.5$ in the vicinity of T_c), $g(E) = E/[E^2\text{-}\Delta(T)^2]^{0.5}$ represents the single quasiparticle DOS in the BCS theory, and $f'(E)$ is the derivative of the Fermi-Dirac distribution [15–17]. As shown in Eq. (3), with the integral of the product of $g(E)$ and $f'(E)$, we realize the removal of single quasiparticles around the Fermi energy from the fermionic channel for the formation of isolated localized Cooper pairs below T_c^{onset}(local). To describe the intergrain resistivity, the universal formula for Mott insulators is applied

$$\rho_{inter} = \rho_r \exp\left\{\left(\frac{T_0}{T}\right)^{\alpha}\right\}. \tag{3}$$

For the empirical modeling of ρ_B, a power law is used to approximate the bosonic condensation in the resistor network at T_c^{offset}

$$\rho_B = \rho_0 + \rho_s\left(\frac{T}{T_c^{offset}} - 1\right)^{\eta}, \tag{4}$$

where η, together with ρ_s, characterizes the efficiency of the intergrain Josephson coupling (establishment of the percolation path for Cooper pairs) in the presence of granular disorder. ρ_0 is introduced when no percolation path across the resistor network but only local phase coherence is established under pressure. In this case, the system cannot reach the superconducting state ($\rho = 0$) [17].

The total resistivity ρ_{total} of the series-parallel circuit is

$$\rho_{total} = \frac{\rho_F\rho_B}{\rho_F + \rho_B} = \frac{(\rho_{intra} + \rho_{inter})\rho_B}{\rho_{intra} + \rho_{inter} + \rho_B}. \tag{5}$$

To perform the theoretical modeling, T_c^{onset}(local) = 7 K is fixed for all the $\rho(T)$ curves measured under different pressures, T_c^{offset} = 2.3 K is fixed for the $\rho(T)$ curve without pressure, and ρ_n, ρ_0, ρ_s, ρ_r, Δ_0, ω, η, α, and T_0 are left as fitting parameters, together with the T_c^{offset} of the $\rho(T)$ curves under high pressures. Due to the switch-like function of the circuit, the two channels dominate in different temperature ranges (when $\rho_F \gg \rho_B$, the bosonic channel dominates over the fermionic channel, and *vice versa*). Equations (2) and (3) with fitting parameters of ρ_n, ρ_r, Δ_0, ω, α, and T_0 are aimed at modeling the $\rho(T)$ increase prior to the resistive superconducting transition, which overshoots the exponential law [see Fig. 4(b)]. Equation (4) with fitting parameters of ρ_0, ρ_s, T_c^{offset}, and η provides an empirical modeling of the effects of bosonic condensation. The competition between these three mechanisms results in the $\rho(T)$ maximum. As

TABLE I. Variables used for modeling the pressure-tuned superconductor-insulator transition in heavily boron-doped nanodiamond thin films with the series-parallel circuit.[a]

P (GPa)	ρ_n ($\mu\Omega$ m)	Δ_0 (meV)	ω	ρ_s ($\mu\Omega$ m)	ρ_0 ($\mu\Omega$ m)	η	ρ_r ($\mu\Omega$ m)	α	T_0 (K)	T_c^{offset} (K)
0	11.7	0.14	0.14	854.3	0	1.98	0	–	–	2.3
2.4	5	0.35	0.38	171.6	25.9	0.82	4.4	0.03	11	2.1
9.2	4	0.44	0.6	160.5	60.9	0.98	7.8	0.06	12	1.9
11.2	3.9	0.5	0.45	183	64.5	1.13	9.3	0.05	15	1.7
12.2	4.9	0.45	0.51	424	146	1.2	15	0.05	17	1.6
16	5.7	0.51	0.49	286	97	1.25	17.8	0.05	18	1.4
19.2	6.1	0.51	0.43	527	175	1.41	27.4	0.05	20	1.3

[a]The pressure P, fixed for different experiments, is used to label the datasets, while other variables are left as free parameters for fitting. A Levenberg-Marquardt routine is used to perform the least-squares fitting.

shown in Fig. 5(c), our series-parallel circuit model reproduces reasonably well the observed $\rho(T)$ behavior under different pressures.

The resulting fitting parameters are shown in Table I. At zero pressure, ρ_{inter} is eliminated from the fermionic channel due to $\rho_r = 0$, indicating that the proximity coupling between the nanodiamond grains enables the establishment of a percolation path and thus the emergence of the superconducting state ($\rho = 0$). Along with the increase of the applied pressure, ρ_{inter} becomes dominant in its competition with ρ_{intra} as revealed by the ratio of ρ_r to ρ_n. The increased weight of ρ_{inter} is indicative of pressure-induced deformations/cracks at the grain boundaries and thus the suppression of the intergrain Josephson coupling. The overall increase of ρ_0 with an exception of the 16-GPa data, and the decrease of T_c^{offset} indicate the breaking of the percolation path under pressures. A linear fit to the T_c^{offset}-P plot yields a slope of -0.05 K/GPa, which is slightly smaller than the values of -0.064 K/GPa reported for the midpoint T_c of polycrystalline bulk diamond and -0.09 K/GPa for T_c^{offset} of 60-μm-thick diamond film [5,14]. In Ref. [14], the negative pressure coefficient of T_c was attributed to a decrease of the electron-phonon coupling parameter, while we point out the essential relevance of pressure-induced deformations/cracks at the grain boundaries in our much thinner nanodiamond films.

Our picture suggests that the applied pressure should slow down the resistive superconducting transition by increasing the disorder degree of the resistor network. This expectation is, however, not supported by a monochromatic decrease of ρ_s or η. When fitting the $\rho(T)$ curves under high pressures, Eq. (4) still tends to compete with Eqs. (3) and (2) for reproducing the rather limited $\rho(T)$ decrease caused by local phase coherence at low temperatures, which gives rise to the increased ρ_s and η (see Table I). This mathematical competition contradicts our picture and does not hold in physics, because the overall insulating state emerges along with the destruction rather than the development of the percolation path for Cooper pairs. The shortcoming of our model is also reflected by the distinct mismatch between the experimental result and the fitting value of Δ_0. These misfits probably result from our simplification of the disordered system into the series-parallel circuit, where different nanodiamond grains and various grain boundary conditions are described with the same set of parameters. Taking Δ_0 and T_c^{onset}(local) for example, despite the rather homogeneous boron doping, granular diamonds generally demonstrate strong modulations of the local superconducting order parameter, and the opening of the local superconducting gap can even take place below T_c^{offset} [16,25,33]. Despite the shortcomings mentioned above, we emphasize that, in contrast to the majority of previous theories that only cover a part of the resistive superconducting transition, our model takes into account the fingerprint of the superconducting transition in granular disordered systems, i.e., the $\rho(T)$ maximum, and reproduces the entire transition reasonably well.

V. CONCLUSION

By introducing the high-pressure technique into the research on electronic properties of heavily boron-doped nanodiamond thin films, we are able to tune the intergrain coupling and thus the intragrain confinement of single quasiparticles and Cooper pairs. As a result of the suppressed intergrain tunneling by pressure, an increase in the normal-state resistivity and a superconductor-insulator transition are observed in our nanodiamond films. The superconductor-insulator transition is interpreted in the framework of a series-parallel circuit model. Our data provide evidence for the percolative nature of the electrical transport, and reveal the essential role of grain boundaries in determining the electronic properties of this material. Our model, developed for nanodiamond thin films, can be applied to general granular disordered superconductors.

ACKNOWLEDGMENTS

Y.Z. and Z.Y. acknowledge support from the National Key Research and Development Program of China (Grants No. 2018YFA0305700 and No. 2016YFA0401804), the National Natural Science Foundation of China (Grants No. 11574323, No. 11704387, and No. U1632275), the Natural Science Foundation of Anhui Province (Grants No. 1708085QA19 and No. 1808085MA06), and the Director's Fund of Hefei Institutes of Physical Science, Chinese Academy of Sciences (YZJJ201621). J.V. and S.K. acknowledge funding from the GOA project "Solarpaint" of the University of Antwerp, and thank the FWO (Research Foundation-Flanders) for financial support under Contract No.

G.0044.13N "Charge ordering". The Qu-Ant-EM microscope was partly funded by the Hercules fund from the Flemish Government. T.S., O.O., and P.S. are supported by APVV-0036-11, APVV-0605-14, VEGA 1/0409/15, VEGA 2/0149/16, and EU ERDF-ITMS 26220120005. L.L. acknowledges the financial support of a FWO postdoctoral research fellowship (12V4419N) and the KU Leuven C1 project OPTIPROBE (C14/16/063).

[1] P. W. May, Diamond thin films: A 21st-century material, Phil. Trans. R. Soc. Lond. A **358**, 473 (2000).

[2] J. E. Butler and R. L. Woodin, Thin film diamond growth mechanisms, Philos. Trans. R. Soc. London, Ser. A **342**, 209 (1993).

[3] M. Syamsul, Y. Kitabayashi, D. Matsumura, T. Saito, Y. Shintani, and H. Kawarada, High voltage breakdown (1.8 kV) of hydrogenated black diamond field effect transistor, Appl. Phys. Lett. **109**, 203504 (2016).

[4] J. Kusterer, E. Kohn, A. Lu¨ker, P. Kirby, and M. F. O'Keefe, Diamond high speed and high power MEMS switches, in *Proceedings from the 4th EMRS DTC Technical Conference, July 10–11, 2007, Edinburgh, UK* (EMRS DTC, Edinburgh, UK, 2007), p. A26.

[5] E. A. Ekimov, V. A. Sidorov, E. D. Bauer, N. N. Mel'nik, N. J. Curro, J. D. Thompson, and S. M. Stishov, Superconductivity in diamond, Nature (London) **428**, 542 (2004).

[6] Y. Takano, M. Nagao, I. Sakaguchi, M. Tachiki, T. Hatano, K. Kobayashi, H. Umezawa, and H. Kawarada, Superconductivity in diamond thin films well above liquid helium temperature, Appl. Phys. Lett. **85**, 2851 (2004).

[7] S. Mandal, T. Bautze, O. A. Williams, C. Naud, E. Bustarret, F. Omnès, P. Rodière, T. Meunier, C. Bäuerle, and L. Saminadayar, The diamond superconducting quantum interference device, ACS Nano **5**, 7144 (2011).

[8] E. Bustarret, Superconductivity in doped semiconductors, Physica C **514**, 36 (2015).

[9] X. Blase, E. Bustarret, C. Chapelier, T. Klein, and C. Marcenat, Superconducting group-IV semiconductors, Nat. Mater. **8**, 375 (2009).

[10] G. Baskaran, Resonating valence bond mechanism of impurity band superconductivity in diamond, J. Supercond. Nov. Magn. **21**, 45 (2008).

[11] T. Klein, P. Achatz, J. Kacmarcik, C. Marcenat, F. Gustafsson, J. Marcus, E. Bustarret, J. Pernot, F. Omnes, Bo E. Sernelius, C. Persson, A. Ferreira da Silva, and C. Cytermann, Metal-insulator transition and superconductivity in boron-doped diamond, Phys. Rev. B **75**, 165313 (2007).

[12] D. Kumar, M. Chandran, D. K. Shukla, D. M. Phase, K. Sethupathi, and M. S. Ramachandra Rao, $T_c$suppression and impurity band structure in overdoped superconducting boron-doped diamond films, Physica C **555**, 28 (2018).

[13] J. Bousquet, T. Klein, M. Solana, L. Saminadayar, C. Marcenat, and E. Bustarret, Phase diagram of boron-doped diamond revisited by thickness-dependent transport studies, Phys. Rev. B **95**, 161301(R) (2017).

[14] M. Abdel-Hafiez, D. Kumar, R. Thiyagarajan, Q. Zhang, R. T. Howie, K. Sethupathi, O. Volkova, A. Vasiliev, W. Yang, H. K. Mao, and M. S. Ramachandra Rao, High-pressure behavior of superconducting boron-doped diamond, Phys. Rev. B **95**, 174519 (2017).

[15] G. Zhang, M. Zeleznik, J. Vanacken, P. W. May, and V. V. Moshchalkov, Metal–Bosonic Insulator–Superconductor Transition in Boron-Doped Granular Diamond, Phys. Rev. Lett. **110**, 077001 (2013).

[16] G. Zhang, T. Samuely, J. Kačmarčík, E. A. Ekimov, J. Li, J. Vanacken, P. Szabó, J. Huang, P. J. Pereira, D. Cerbu, and V. V. Moshchalkov, Bosonic Anomalies in Boron-Doped Polycrystalline Diamond, Phys. Rev. Appl. **6**, 064011 (2016).

[17] G. Zhang, T. Samuely, H. Du, Z. Xu, L. Liu, O. Onufriienko, P. W. May, J. Vanacken, P. Szabó;, J. Kačmarčík, H. Yuan, P. Samuely, R. E. Dunin-Borkowski, J. Hofkens, and V. V. Moshchalkov, Bosonic confinement and coherence in disordered nanodiamond arrays, ACS Nano **11**, 11746 (2017).

[18] G. Zhang, S. Janssens, J. Vanacken, M. Timmermans, J. Vacík, G. W. Ataklti, W. Decelle, W. Gillijns, B. Goderis, K. Haenen, P. Wagner, and V. V. Moshchalkov, Role of grain size in superconducting boron-doped nanocrystalline diamond thin films grown by CVD, Phys. Rev. B **84**, 214517 (2011).

[19] L. Dubrovinsky, N. Dubrovinskaia, V. B. Prakapenka, and A. M. Abakumov, Implementation of micro-ball nanodiamond anvils for high-pressure studies above 6 Mbar, Nat. Commun. **3**, 1163 (2012).

[20] O. J. L. Fox, J. O. P. Holloway, G. M. Fuge, P. W. May, M. N. R. Ashfold, Electrospray deposition of diamond nanoparticle nucleation layers for subsequent CVD diamond growth, in *Diamond Electronics and Bioelectronics - Fundamentals to Applications III*, edited by P. Bergonzo, J. E. Butler, R. B. Jackman, K. P. Loh, and M. Nesladek (Mater. Res. Soc. Symp. Proc. Warrendale, PA, 2010), Vol. 1203, pp. J17-27.

[21] H. K. Mao, J. Xu, and P. M. Bell, Calibration of the ruby pressure gauge to 800 kbar under quasi-hydrostatic conditions, J. Geophys. Res. **91**, 4673 (1986).

[22] T. Samuely, P. Szabó, V. Komanický, J. G. Rodrigo, S. Vieira, and P. Samuely, Enhanced superconductivity in nano-sized tips of scanning tunneling microscope, Acta Phys. Pol. A **118**, 1038 (2010).

[23] M. Tinkham, *Introduction to Superconductivity* (Dover, New York, 2004), pp. 75–76.

[24] E. Bustarret, P. Achatz, B. Sacépé, C. Chapelier, C. Marcenat, L. Ortéga, and T. Klein, Metal-insulator transition and superconductivity in boron-doped diamond, Philos. Trans. R. Soc. A **366**, 267 (2008).

[25] G. Zhang, S. Turner, E. A. Ekimov, J. Vanacken, M. Timmermans, T. Samuely, V. A. Sidorov, S. M. Stishov, Y. Lu, B. Deloof, B. Goderis, G. Van Tendeloo, J. Van de Vondel, and V. V. Moshchalkov, Global and local superconductivity in boron-doped granular diamond, Adv. Mater. **26**, 2034 (2014).

[26] B. Abeles, Effect of charging energy on superconductivity in granular metal films, Phys. Rev. B **15**, 2828 (1977).

[27] Y. Shapira and G. Deutscher, Semiconductor-superconductor transition in granular Al-Ge, Phys. Rev. B **27**, 4463 (1983).

[28] H. M. Jaeger, D. B. Haviland, B. G. Orr, and A. M. Goldman, Onset of superconductivity in ultrathin granular metal films, Phys. Rev. B **40**, 182 (1989).

[29] G. Zhang, J. Vanacken, J. Van de Vondel, W. Decelle, J. Fritzsche, V. V. Moshchalkov, B. L. Willems, S. D. Janssens, K. Haenen, and P. Wagner, Magnetic field-driven superconductor-insulator transition in boron-doped nanocrystalline chemical vapor deposition diamond, J. Appl. Phys. **108**, 013904 (2010).

[30] P. Achatz, W. Gajewski, E. Bustarret, C. Marcenat, R. Piquerel, C. Chapelier, T. Dubouchet, O. A. Williams, K. Haenen, J. A. Garrido, and M. Stutzmann, Low-temperature transport in highly boron-doped nanocrystalline diamond, Phys. Rev. B **79**, 201203(R) (2009).

[31] G. M. Klemencic, J. M. Fellows, J. M. Werrell, S. Mandal, S. R. Giblin, R. A. Smith, and O. A. Williams, Fluctuation spectroscopy as a probe of granular superconducting diamond films, Phys. Rev. Mater. **1**, 044801 (2017).

[32] D. L. Creedon, Y. Jiang, K. Ganesan, A. Stacey, T. Kageura, H. Kawarada, J. C. McCallum, B. C. Johnson, S. Prawer, and D. N. Jamieson, Irradiation-Induced Modification of the Superconducting Properties of Heavily-Boron-Doped Diamond, Phys. Rev. Appl. **10**, 044016 (2018).

[33] F. Dahlem, P. Achatz, O. A. Williams, D. Araujo, E. Bustarret, and H. Courtois, Spatially correlated microstructure and superconductivity in polycrystalline boron-doped diamond, Phys. Rev. B **82**, 033306 (2010).